

Shear margin interaction and ramifications for ice stream stability at Institute Ice Stream, West Antarctica

C. W. Elsworth¹, and J. Suckale^{1,2}

¹Department of Geophysics, Stanford University, USA

²Institute for Computational and Mathematical Engineering, Stanford University, USA

Key Points:

- We develop a general anti-flow line model for analyzing ice-stream stability in field settings.
- The slowly-sliding marginal zone connects grounding line processes to ice-stream dynamics.
- Increased melt rates could alter ice-stream dynamics prior to grounding line retreat.

12 **Abstract**

13 Many ice streams in West Antarctica move over spatially heterogeneous beds with variable
 14 topography, lithology and hydrology. Radio-echo sounding surveys across the ice sheets in-
 15 creasing illustrate that heterogeneity in the subglacial conditions is the norm rather than the
 16 exception. In contrast, most process-based models assume simplistic homogeneous domains
 17 to isolate the effect of a single process. Currently, there are few model approaches that ex-
 18 plicitly consider variable, mixed bed conditions, which limits our ability to apply process-
 19 based models to specific field sites. Here, we develop a free-boundary model of ice sliding
 20 over a mixed bed by adding lithologic, topographic, and hydrological complexity to create an
 21 anti-plane flow model for studying shear margins. By focusing on the cross-sectional force
 22 balance of ice streams, our approach is a complement to the commonly used flow-line mod-
 23 els. We apply our model to Institute Ice Stream, which flows into the Weddell Sea Sector,
 24 Antarctica. Institute Ice Stream is interesting, because of its dynamic past and uncertain fu-
 25 ture in light of a projected increase in melt rates in the Weddell Sea Sector. Extensive air-
 26 borne surveys provide detailed observations of heterogeneous bed conditions with one shear
 27 margin underlain by hardrock and the other by soft sediments. Our model demonstrates that
 28 slow slip in the western ridge of Institute could play an important dynamic role in the evolv-
 29 ing dynamics of the ice stream, because it couples processes in the vicinity of the grounding
 30 line to the main ice trunk. Our analysis suggests that increase melt rates at the grounding line
 31 could alter the dynamics of Institute ice stream prior to actual retreat of the grounding line.

32 **1 Introduction**

33 Fast-moving outlet glaciers and ice streams account for the majority of mass loss from
 34 the Antarctic continent [Bamber *et al.*, 2000]. While ultimately a fluent transition, outlet
 35 glaciers and ice streams vary by the degree to which they are controlled by varying topog-
 36 raphy at the bed. The lateral shear margins of ice streams do not correlate with distinct to-
 37 graphic features of the bed as clearly as is the case for outlet glaciers [Raymond, 2000;
 38 Truffer and Echelmeyer, 2003]. The reduced topographic control on ice streams means that
 39 they are inherently dynamic features and sensitively dependent on evolving subglacial condi-
 40 tions [Raymond, 2000; Truffer and Echelmeyer, 2003; Winsborrow *et al.*, 2010].

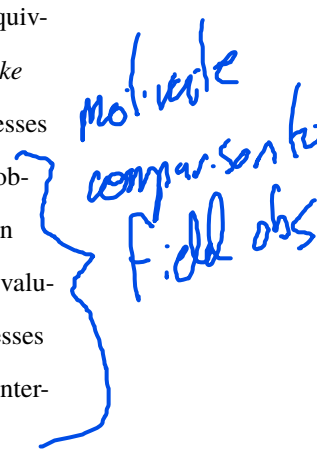
41 Previous models have improved our understanding of how thermal [Schoof, 2004,
 42 2012; Suckale *et al.*, 2014; Perol *et al.*, 2015; Haseloff *et al.*, 2015], and hydrological [Perol
 43 and Rice, 2015; Platt *et al.*, 2016; Elsworth and Suckale, 2016a] processes at the base of the

*Interesting
sort of
features,
is it
Binary?*

44 ice contribute to the stability of shear margins. Most of these models consider highly ide-
 45 alized ice streams sliding over a homogeneous bed, inspired by the Siple Coast Ice Streams
 46 that are characterized by low topography and widespread sediment deposits [e.g., Perol *et al.*,
 47 2015; Suckale *et al.*, 2014; Elsworth and Suckale, 2016a]. In many other regions, the com-
 48 plexity of the underlying substrate and topography play an important role [e.g., Macgregor
 49 *et al.*, 2013]. This heterogeneity in subglacial conditions likely contributes to a wide spec-
 50 trum of observed ice-stream dynamics [e.g., Raymond, 1996, 2000; Truffer and Echelmeyer,
 51 2003], but little progress has been made in quantifying that link.

52 The goal of this study is to advance our ability to assess the stability of ice streams
 53 sliding over heterogeneous subglacial beds by generalizing existing, idealized models to
 54 improve applicability to field sites. We develop a thermo-mechanical model for the cross-
 55 section of an ice stream that includes a free-boundary formulation to determine the evolving
 56 slip interface at the ice-bed interface, following Schoof [2006a]. The free-boundary formu-
 57 lation allows us to determine the regions of sediment failure at the ice-bed interface self-
 58 consistently from an integrated force balance rather than imposing shear-margin position *a*
 59 *priori*. The model setup allows for complex geometries, and subglacial boundary conditions
 60 representative of perfectly plastic sediment behavior [Tulaczyk *et al.*, 2000; Kamb, 2001],
 61 velocity-strengthening hard rock sliding laws [Weertman, 1957], and regularized Coulomb
 62 sliding over hard rock [Schoof, 2005].

63 We refer to our approach as an anti-flow-line model, because it is the anti-plane equiv-
 64 alent of the more commonly applied flow-line models pioneered in the 1980s [e.g., Hooke
 65 *et al.*, 1979; ?; ?]. Our forward model computes the surface signatures of physical processes
 66 occurring at the subglacial interface. By comparing the model results to actual surface ob-
 67 servables, we can eliminate subglacial processes that are incompatible with data. We can
 68 also identify the locations and types of field measurements that would provide the most val-
 69 uable constraints from a modeling point of view. To narrow the range of subglacial processes
 70 we consider in our simulations, we rely on remotely-sensed data constraining the basal inter-
 71 face to select reasonable subglacial conditions.



72 The resolution of remotely-sensed data probing the ice sheets has increased substan-
 73 tially in recent years [Schroeder *et al.*, 2014; Siegert *et al.*, 2016; Muto *et al.*, 2019; Koellner
 74 *et al.*, 2019]. Radio-echo sounding [Schroeder *et al.*, 2014; Siegert *et al.*, 2016] and seis-
 75 mic [Muto *et al.*, 2019; Koellner *et al.*, 2019] surveys have advanced our ability to map out

76 heterogeneity in subglacial conditions. These increasingly detailed observations highlight
 77 that heterogeneity in basal conditions is the norm rather than the exception. The observed
 78 diversity is not surprising in light of the numerous physical processes at play in a heteroge-
 79 neous subglacial environment [Schroeder *et al.*, 2014; Siegert *et al.*, 2016; Muto *et al.*, 2019;
 80 Koellner *et al.*, 2019]. Increasingly detailed observations provide an important opportunity
 81 for models to better constrain the relative importance of the various physical processes that
 82 contribute to the dynamics of ice streams and their shear margins.

83 To integrating site-specific, high-resolution data into our analysis, we focus on Institute
 84 Ice Stream, West Antarctica (see Figure 1a). Institute Ice Stream represents a field setting
 85 of intermediate complexity that shares similarities with the Siple Coast such as low over-
 86 all driving stresses and a widespread, unconsolidated sediment layer [Bingham and Siegert,
 87 2007]. Radio-echo sounding surveys map out a mildly varying topography and suggest the
 88 existence of a distinct transition between hardrock and saturated sediments underneath the
 89 ice stream [Siegert *et al.*, 2016]. From a dynamic point of view, Institute Ice Stream has
 90 attracted attention because it is located on a reverse-sloping bed with few pinning points
 91 [Bingham and Siegert, 2007; Ross *et al.*, 2012], making it prone to the marine ice-sheet in-
 92 stability [Weertman, 1974; Thomas, 1979; Schoof, 2007; Jamieson *et al.*, 2012].

93 The marine ice-sheet instability could be initiated by melting at the grounding line,
 94 which is currently concentrated in the Amundsen Sea Sector [Joughin *et al.*, 2014; Rig-
 95 not *et al.*, 2014; Milillo *et al.*, 2019], but could reach the Weddell Sea Sector later this cen-
 96 tury [Hellmer *et al.*, 2012]. Most previous model efforts have focused on understanding
 97 grounding-line melting [Wright *et al.*, 2014] in the Weddell Sea Sector. Here, we focus on
 98 better constraining the potential dynamic response of Institute Ice Stream to the projected in-
 99 crease in melting based the extensive geophysical surveys that have previously been acquired
 100 at Institute [Jordan *et al.*, 2013; Siegert *et al.*, 2013, 2016]. An analysis of internal layering
 101 at Institute Ice Stream has revealed flow-path rearrangement and retreat, highlighting its dy-
 102 namic history and potential to evolve rapidly in the future [Siegert *et al.*, 2013; Winter *et al.*,
 103 2015].

*Read History
Read papers!*

114 2 Field setting of Institute Ice Stream

115 Institute Ice Stream is located in the Ronne Ice Shelf region of West Antarctica, shown
 116 in Figure 1a. It has been studied extensively due to its reverse-slope bed with few pinning

points, low basal resistance to ice flow, and dynamic history of rearrangement [Bingham and Siegert, 2007; Ross *et al.*, 2012; Siegert *et al.*, 2013]. The streaming ice is bounded on the East by Bungenstock Ice Rise, and fed from the West by tributaries from the Ellsworth Mountains [Ross *et al.*, 2011, 2014]. The two shear margins at Institute exhibit different surface expressions, with the Western shear margin being much less localized than the Eastern shear margin [Scambos *et al.*, 2004], shown in Figure 1b.

unsymmetry

Extensive airborne geophysical surveys of the area were completed in the 2010-11 field season by the British Antarctic Survey, including radar sounding, gravity, magnetics, and LIDAR [Jordan *et al.*, 2013]. The geophysical data constrains the various factors that contribute to the dynamics of Institute Ice Stream, including topography, lithology, and hydrology. Siegert *et al.* [2016] highlight subglacial hydrology as an important factor that could induce rapid rearrangement in Institute's trunk. The trunk is downstream from an active subglacial lake, Institute E1 [Smith *et al.*, 2009] highlighted on Figure 1a, and meltwater is emanating from the western shear margin at the grounding line [leB; Alley *et al.*, 2016] in the form of a channel. The hydraulic potential of Institute Ice Stream suggests that subglacial meltwater is routed from the Eastern shear margin to the Western shear margin [Siegert *et al.*, 2016]. The potential for a rapid dynamic response to external forcing is reflected in the ice flow history of the region. Stratigraphy of internal reflectors suggest large-scale rearrangement across Bungenstock Ice Rise as recently as a few centuries ago [Siegert *et al.*, 2013; Winter *et al.*, 2015].

Traditionally, seismic surveys have been used to characterize subglacial lithology at local scales [e.g., Muto *et al.*, 2019]. Alternatively, Siegert *et al.* [2016] develop a technique at Institute to interpret radar sounding profiles and classify subglacial lithology at a catchment-scale. They interpret a transition between subglacial sediments and bedrock topography, shown as a white line in Figure 1a, by thresholding the roughness of the bed. The sharpness of this transition varies between profiles, but appears to be relatively abrupt. Siegert *et al.* [2016] also observe a transition in bed return power between the streaming portion of Institute and Bungenstock Ice Rise, which they interpret as a transition from frozen to wet sediments underneath the Eastern shear margin [Siegert *et al.*, 2016]. A radar cross-section for the survey most perpendicular to flow, Profile C-C', is shown in Figure 1b. These data suggest that the Western shear margin rests on hardrock while the Eastern shear margin is underlain by sediments. The basal topography across this profile is relatively subdued, mak-

149 ing it unlikely that topographic control is the primary factor determining the shear margin
 150 position.

151 **3 Methods**

152 We develop a thermo-mechanical model of an ice stream cross-section oriented per-
 153 perpendicular to flow. Instead of preimposing the margin positions, we solve a free-boundary
 154 problem to identify failure zones based on an integrated force balance across the domain
 155 building on the derivation by *Schoof* [2006a]. We formulate the governing equations of ice
 156 flow for three different subglacial boundary condition representative of failing sediments,
 157 locked sediments, and hard-bed sliding. The free-boundary problem is then converted to, and
 158 solved through the Disciplined Convex Programming framework [*Grant and Boyd*, 2008].
 159 An important contribution of our model is to link the mechanical free-boundary problem as
 160 described in *Schoof* [2006a] to a thermal model in the ice column. The thermal and mechan-
 161 ical model are coupled through a temperature- and strain-rate dependent ice rheology.

162 Previous cross-sectional models addressing the thermomechanical behavior of shear
 163 margins simplify the domain as symmetric and assume uniform basal topography [*Jacob-*
 164 *son and Raymond*, 1998; *Schoof*, 2004; *Suckale et al.*, 2014; *Perol and Rice*, 2015; *Haseloff*
 165 *et al.*, 2015; *Elsworth and Suckale*, 2016a]. Our model setup allows us to include variable to-
 166 *topography*, heterogeneous basal conditions and asymmetric interactions between the two shear
 167 *margins by considering the full ice stream cross-section*, shown in Figure 2. Including these
 168 heterogeneities implies that the plane of antiplane shear stress might not be identical to the
 169 cross-section of the ice stream. We have developed an accompanying algorithm to compute
 170 the appropriate model plane, which we refer to as antiflow line, from surface velocity.

*think about
this*

176 **3.1 Governing Equations**

177 Our free-boundary model extends the mechanical model by *Schoof* [2006a] to include
 178 thermo-mechanical effects. To reduce the complexity of the 3-D geometry, we neglect vari-
 179 ability in the downstream direction ($d/dx \approx 0$), with ice moving in the positive x -direction,
 180 shown in Figure 2b. We assume an anti-plane momentum balance,

$$-\nabla \cdot (\eta(T)|\nabla u|^{1/n-1}\nabla u) = \rho g \sin \alpha \quad \text{on} \quad \Omega, \quad (1)$$

181 with anti-plane velocity, u , temperature-dependent ice viscosity, $\eta(T)$, ice density, ρ , gravitational acceleration, g , and surface slope, α . A typical non-Newtonian Glen's rheology would
 182 entail $n = 3$ [Glen, 1955].
 183

184 The ice thickness is assumed to be constant with a stress-free surface,

$$-\eta(T)|\nabla u|^{1/n-1}u_n = 0 \quad \text{on} \quad \Gamma_{\text{surf}}, \quad (2)$$

185 and that the domain has stress-free lateral bounds,

$$-\eta(T)|\nabla u|^{1/n-1}u_n = 0 \quad \text{on} \quad \Gamma_{\text{lat}}. \quad (3)$$

186 Basal traction is applied at the bed,

$$-\eta(T)|\nabla u|^{1/n-1}u_n = \tau_b(x, y, u) \quad \text{on} \quad \Gamma_{\text{bed}}, \quad (4)$$

such that regions of saturated sediments abide by Coulomb plastic failure,

$$\tau_b = fN + c \quad u > 0 \quad (\text{failing}) \quad (5)$$

$$\tau_b \leq fN + c \quad u = 0 \quad (\text{locked}) \quad (6)$$

187 dependent on effective pressure, $N = \sigma_n - p$, where σ_n is the overburden, p the pore pressure,
 188 f the friction factor, and c the sediment cohesion. For the portion of the subglacial bed that
 189 consists of hardrock, we assume that the basal traction follows a sliding law,

$$\tau_b = \beta^2|u|^m \quad (7)$$

190 dependent on a power law relationship of anti-plane ice velocity, u . This sliding law can rep-
 191 resent three different regimes: velocity-strengthening behavior, $m > 0$, as might arise when
 192 sliding over bumps without cavitation [e.g., Weertman, 1957]; velocity-weakening behav-
 193 ior, $m < 0$, potentially indicative of bed bumps with cavitation [e.g., Lliboutry, 1968]; and
 194 regularized Coulomb sliding over hard rock, $m = 0$ [e.g., Schoof, 2005]. Out of these three
 195 possibilities, velocity-weakening behavior [Lliboutry, 1968; Zoet and Iverson, 2016] with
 196 $m < 0$, is difficult to stabilize in our model when applied to the entire or most of the hardrock
 197 bed. We hence do not consider this limit in our simulations.

198 We assume that the temperature distribution in the ice column is driven by diffusion of
 199 shear heating,

$$-\nabla \cdot (k \nabla T) = 2\tau_E(u)\dot{\epsilon}_E(u), \quad T < T_{\text{melt}}, \quad (8)$$

Is this true?

200 with thermal conductivity, k , effective stress, $\tau_E(u)$, effective strain rate, $\dot{\epsilon}_E(u)$, and pressure
 201 melting point, T_{melt} . The boundary conditions are a fixed surface temperature, T_s ,

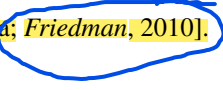
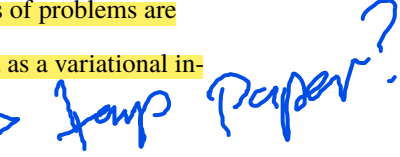
$$T = T_s \quad \text{on} \quad \Gamma_{\text{surf}}, \quad (9)$$

202 periodic lateral bounds,

$$-k\nabla T = 0 \quad \text{on} \quad \Gamma_{\text{lat}}, \quad (10)$$

203 and constant geothermal heat flux, G_{geo} , at the bed,

$$-k\nabla T = G_{\text{geo}} \quad \text{on} \quad \Gamma_{\text{bed}}. \quad (11)$$

204 The primarily difficulty in solving these governing equations arises from the unknown
 205 location and extent of the slip zone that determines where the different boundary conditions
 206 of the mechanical model are applied and where shear heating is concentrated in the thermal
 207 model. In the mechanical model, sliding over a perfectly-plastic bed abruptly transitions
 208 from locked (fixed-value) to failing (fixed-gradient) based on the integrated force-balance
 209 of the ice stream. Without the location of the transition points known *a priori*, the solution
 210 of the governing equations includes both the solution field and the location of the bound-
 211 ary conditions. Similarly, for the thermal model shear heating occurs until the melting point
 212 is reached, without regions of temperate ice known *a priori*. These types of problems are
 213 known as free-boundary, partial differential equations, and can be solved as a variational in-
 214 equality [Schoof, 2006a; Friedman, 2010].  

The variational form of the mechanical free-boundary is developed in Schoof [2006a].

In the interest of completeness, we briefly summarize the main idea and key equations in Appendix A. In the variational formulation, solving the anti-plane momentum balance, eq. 1, becomes equivalent minimizing the energy functional, $J(u)$, subject to the constraint that flow occurs only in the downstream direction:

$$\text{minimize} \quad J(u) = \frac{1}{p} \int_{\Omega} \eta(T) |\nabla u|^p + \int_{\Gamma_{\text{bed}}} \tau_b |u| - \int_{\Omega} \rho g \sin \alpha u \quad (12)$$

$$\text{subject to} \quad u \geq 0. \quad (13)$$

215 In the interest of a succinct notation, we set $p = 1 + 1/n$. The energy functional, $J(u)$, has
 216 been proven to be convex in $v \geq 0$, and unique when a solution exists [Schoof, 2006a].

We use the same method to develop a variational inequality for englacial temperature in the domain as derived in more detail in Appendix B. We define the thermal energy functional, $L(T)$, which we minimize subject to the constraint that the temperature can not exceed

the pressure melting point,

$$\text{minimize} \quad L(T) = \frac{1}{2} \int_{\Omega} k |\nabla T|^2 - \int_{\Gamma_{\text{bed}}} G_{\text{geo}} T - \int_{\Omega} 2\tau_E(u) \dot{\epsilon}_E(u) T \quad (14)$$

$$\text{subject to} \quad T \leq T_{\text{melt}}. \quad (15)$$

Our model extends the approach of [Meyer and Minchew \[2018\]](#), a one-dimensional free-boundary analytical solution for [the temperature field in an ice column, to two dimensions](#).

3.2 Numerical Method

We have reformulated the initial governing equations as a set of constrained minimizations problems that are convex in the anti-plane velocity, u , and temperature, T . For a given domain, we solve these [optimization problems by discretizing the domain and solving the convex minimization numerically](#). We begin by discretizing the mechanical energy functional, described by Equation A.6 on a domain, Ω , with an arbitrary triangulation consisting of elements, τ , and boundary edges, γ ,

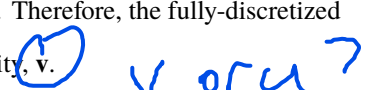
$$J(u) = \frac{1}{p} \sum_{\tau} \int_{\tau} \eta(T) |\nabla u|^p + \sum_{\gamma} \int_{\gamma} \tau_b |u| - \sum_{\tau} \int_{\tau} \rho g \sin \alpha u. \quad (16)$$

Choosing a piecewise-linear basis, ϕ_i , on each element, with nodal weight function, v_i , the semi-discretized energy functional becomes

$$J(u_i) = \frac{1}{p} \sum_{\tau} \eta(T) \int_{\tau} \left| \sum_{i=1}^3 u_i \nabla \phi_i \right|^p + \sum_{\gamma} \sum_{i=1}^2 u_i \int_{\gamma} \tau_b \phi_i - \rho g \sin \alpha \sum_{\tau} \sum_{i=1}^3 u_i \int_{\tau} \phi_i. \quad (17)$$

The next step is to fully discretize each term of the energy functional, while ensuring that each term follows the convex composition rules of Disciplined Convex Programming [[Grant and Boyd, 2008](#)]. Disciplined Convex Programming is a framework to specify convex minimization problems algorithmically, which can then be solved by generalized, efficient numerical methods. The process of verifying convex composition is outlined in the Appendix, but the resulting vectorized, fully-discretized energy becomes,

$$J(\mathbf{u}) = \frac{1}{p} (\boldsymbol{\eta}(T) \circ \mathbf{d}\boldsymbol{\tau})^T \|[\mathbf{D}_x \mathbf{u}, \mathbf{D}_y \mathbf{u}]\|^p + (\mathbf{d}\boldsymbol{\gamma} \circ \boldsymbol{\tau}_b)^T \mathbf{u}_b - (\mathbf{d}\boldsymbol{\tau} \circ \mathbf{f})^T \mathbf{u}, \quad (18)$$

with descretized gradient operators, \mathbf{D}_x and \mathbf{D}_y , elementwise multiplication, \circ , boundary nodal values, \cdot_b , and second-dimension vector-wise norm, $\|\cdot\|$. Therefore, the fully-discretized energy functional is a convex function on the vectorized velocity, \mathbf{v} . 

237 A similar process is performed on the thermal minimization problem, resulting in a
 238 vectorized, fully-discretized energy,

$$L(\mathbf{T}) = \frac{1}{2}(\mathbf{k} \circ \mathbf{d}\tau)^T \left\| [\mathbf{D}_x \mathbf{T}, \mathbf{D}_y \mathbf{T}] \right\|^2 + G_{\text{geo}} \mathbf{dy}^T \mathbf{u}_b - (\mathbf{d}\tau \circ \tau_E(\mathbf{T}) \dot{\epsilon}_E(\mathbf{u}))^T \mathbf{T}, \quad (19)$$

239 Each minimization problem is solved through the Disciplined Convex Programming software
 240 library, CVX [Grant and Boyd, 2008, 2013].

241 The governing equations are coupled through the temperature-dependent ice viscos-
 242 ity, $\eta(T)$, and viscous shear heating, $2\tau_E(u)\dot{\epsilon}_E(u)$. We perform this coupling through under-
 243 relaxed Newton-Raphson iteration between the thermal and mechanical models, shown in
 244 Figure 3. At each iteration, the thermal solution is relaxed by a relaxation parameter, $\omega =$
 245 $[0, 1]$, and iterations are performed until the iteration residual is below a threshold, ϵ . The
 246 result of this coupling is a anti-plane velocity, u , and temperature field, T , that are fully-
 247 consistent.

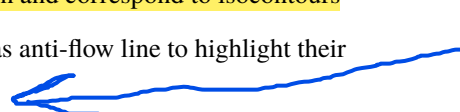
252 3.3 Verification of the Mechanical Model

253 To verify the accuracy of our implementation of the mechanical model, we bench-
 254 mark it against the solution of an idealized valley glacier from Schoof [2006a]. This test
 255 case consists of a simplified valley glacier geometry underlain by saturated sediments, with
 256 variable pore pressure resulting from a specified water table elevation. Distinct failure re-
 257 gions become apparent when the water table elevation and driving stress are varied. Fig-
 258 ure 4a shows the model set-up of a triangular computational domain, with water table eleva-
 259 tion denoted by a dashed line, and failure patches shown as red. In Figure 4a, we reproduce
 260 Figure 5 from Schoof [2006a] with the developed method by simulating the four distinct fail-
 261 ure regimes. We demonstrate that our solver using a nominal grid spacing of $\Delta x = 0.02$ re-
 262 produces the velocity field and failure patches of Schoof [2006a]. Small deviations between
 263 these two solutions likely results from differences in discretization parameters.

264 We perform a numerical convergence analysis of the developed method for each of
 265 these benchmark solutions, shown in Figure 4b. The normalized L_2 -error of surface veloc-
 266 ities, computed against the most refined simulation, exhibit second-order convergence with
 267 grid refinement. The order of accuracy of the linear finite elements is first-order, $p = 1$, with
 268 an expected $p + 1$, or second-order, numerical convergence rate [Brenner and Scott, 2007].
 269 The observed second-order numerical convergence makes us confident that our implemen-
 270 tation of the numerical method is correct and consistent. We are not aware of a verification

271 case of a thermomechanically-coupled free-boundary problem that would allow us to per-
272 form a similar analysis for thermally variable ice.

279 3.4 Computation of anti-flow lines

280 Contrary to many Siple Coast Ice Streams, the flow geometry of Institute Ice Stream
281 is sufficiently complex such that flow in a simple linear transect through both shear margins
282 does not abide by the anti-plane flow assumption. To compare our model results to InSAR-
283 derived velocity data at Institute [Rignot *et al.*, 2011], \mathbf{u}_d , we numerically generate anti-flow
284 lines that are perpendicular to the main direction of motion and correspond to isocontours
285 of the velocity potential, $\phi(\nabla\phi = \mathbf{u}_d)$. We refer to these as anti-flow line to highlight their
286 identification through the assumption of anti-plane shear. 

287 Noise in the observed velocity field violates the irrotational assumption ($\nabla \times \mathbf{u}_d = 0$).
288 Therefore, we cannot directly solve for velocity potential. Instead, we compute anti-flow
289 lines through numerical integration starting from a seed point in the center of the ice stream,
290 x_0 . Velocity vectors are perpendicular to the anti-flow line, which we generate from the
291 stream center outwards through Euler integration,

$$x_{i+1} = x_i + \Delta x \frac{\mathbf{u}_d^\perp(x_i)}{|\mathbf{u}_d^\perp(x_i)|} \quad (20)$$

292 with step-size, Δx . The resolution of the computation is smaller than the resolution of the
293 observed velocity field, \mathbf{u}_d . This procedure generates an anti-flow line, \mathbf{x} , with finite anti-
294 plane velocity component, and a near-zero in-plane velocity component.

295 3.5 Setup of the model domain for Institute

296 We choose to model a region across the trunk of Institute Ice Stream to leverage exist-
297 ing geophysical data of Siegert *et al.* [2016], specifically the radar profile most perpendicular
298 to flow (C-C') shown in Figure 1b. At this location, the main ice stream trunk is approxi-
299 mately 60 kilometers wide and 1700 meters deep. We simplify the geometry of the actual
300 bed profile by assuming a model domain with a flat surface and a bed that is piecewise lin-
301 ear, neglecting across profile roughness. The driving stress in the region is $f = \rho g H \sin \alpha =$
302 27.5 kPa , with ice density, $\rho = 917 \text{ kg/m}^3$, acceleration due to gravity, $g = 9.8 \text{ m/s}^2$, ice
303 thickness, $H = 1275 \text{ m}$, and surface slope, $\alpha = 0.0024$.

Took up!

No need?

304 Based on the interpretation of radio-echo sounding data, Siegert *et al.* [2016] suggest
 305 that the lithology underneath Institute transitions from sediment to hardrock in the across-
 306 flow direction (see Fig. 1b). Both the bed roughness and return power of the radio-echo
 307 sound provide evidence in favor of this interpretation [Siegert *et al.*, 2016], **but the exact lo-**
 308 **cation of this transition is difficult to pinpoint from the data alone.** We separate the bed into
 309 two boundary conditions specified by regions identified by Siegert *et al.* [2016] as hard rock
 310 and saturated sediments, respectively (see Fig. 1). **We vary the exact location of the litho-**
 311 **logical transition to evaluate whether the radar data by Siegert *et al.* [2016] in conjunction**
 312 **with the large-scale surface velocity measurements of Rignot *et al.* [2011] allow us to better**
 313 **constrain the position of the transition underneath Institute Ice Stream.**

314 As summarized in Figure 1, our study site is characterized by a complex subglacial
 315 drainage system involving a lake upstream[Smith *et al.*, 2009], lateral meltwater drainage in
 316 the main trunk, and a meltwater channel emanating from the grounding line in the vicinity
 317 of the western shear margin [LeBrocq *et al.*, 2013]. Efficient drainage through a subglacial
 318 channel reduces pore pressure in the adjacent bed. We assume that distributed drainage
 319 can be approximated as a thin film of meltwater and that efficient drainage occurs through
 320 a Röthlisberger channel [Röthlisberger, 1972] operating at low pore pressure [Hewitt, 2011;
 321 Perol *et al.*, 2015; Elsworth and Suckale, 2016a]. The reduction in pore pressure depends on
 322 the discharge of the channel and the decay rate of the pressure perturbation scales with the
 323 film thickness of the distributed system as derived in more detail in Perol *et al.* [2015]. We
 324 model the decay of bed strength away from a subglacial drainage located at Y as an exponential
 325 decay in the local pore pressure, p , with coefficient γ ,

$$\tau_c(y) = f \left(\sigma_n - p e^{-|y-Y|/\gamma} \right) + c, \quad (21)$$

326 similar to a prior study of the effect of channelized drainage in shear margins [Elsworth and
 327 Suckale, 2016a]. It is worthwhile to note that the hydrological model we assume here [Perol
 328 *et al.*, 2015] assumes a flat bed while the meltwater channel at Institute is located in a topo-
 329 graphic low, which may alter the spatial scale over which it affects bed properties.

335 4 Results

336 4.1 Anti-flow lines at Institute Ice Stream

337 The classical model of ice streams posits plug-like motion in the trunk of the stream
 338 bordered by two narrow shear margins on the sides [Raymond, 1996], yielding a flow config-

Invert
for fit.

↓
Pan
for this
now

339 uration that is symmetric around the center line of the stream. The corresponding anti-flow
 340 lines would cut linearly across the ice stream, intersecting the two shear margins at a right
 341 angle. The anti-flow lines we compute for Institute Ice Stream based on the InSAR-derived
 342 surface velocity data from *Rignot et al.* [2011] only partially abide by this conceptualiza-
 343 tion (see Fig. 5a). While they are approximately linear in the main trunk, they curve around
 344 to partially align with the main flow direction in the extended marginal zone to the West
 345 of the main trunk (see Fig. 5a). The curvature of the anti-flow lines is the consequence of
 346 partial lateral influx of ice into the main trunk between C and A. It suggests that the across-
 347 stream profile C-C' is dynamically coupled to stresses tens of kilometers further downstream
 348 through an extended marginal zone.

349 To better understand the dynamic implications of an extended marginal zone at Insti-
 350 tute Ice Stream, we focus the remainder of the manuscript on the anti-flow line A-A', because
 351 it aligns most closely with the radar profile C-C' from *Siegert et al.* [2016]. The anti-plane
 352 speed in our model domain is shown in Fig. 5b. In the interest of capturing the entire slip
 353 zone in our model, we use the extended anti-flow line A-A' as our model domain, including
 354 both the ice-stream trunk and the extended marginal zone.

355 Even within the main trunk between the eastern and western shear margin, the pro-
 356 file deviates from the commonly assumed symmetry around the center flow line [Raymond,
 357 1996; Jacobson and Raymond, 1998; Suckale et al., 2014; Perol et al., 2015; Perol and Rice,
 358 2015; Elsworth and Suckale, 2016a]. In the eastern margin, where the trunk borders Bun-
 359 genstock Ice Rise, ice speed transitions from rapid to stationary over a well-defined, local-
 360 ized shear margin of 3 km. The high strain rates and narrow width of the eastern shear mar-
 361 gin at Institute resemble those of the Siple Coast [Suckale et al., 2014; Perol et al., 2015;
 362 Perol and Rice, 2015; Platt et al., 2016; Elsworth and Suckale, 2016a]. In contrast, the west-
 363 ern shear margin is comparatively wide, extending over about 10 km with lower strain rates
 364 throughout. It coincides roughly with a topographic trough (see Fig. 5b), highlighting the
 365 potential importance of topographic controls. Maybe most importantly, the ice stream is not
 366 fully locked outside of the western shear margin, as indicated by a small but finite speed in
 367 the extended marginal zone (see Fig. 5b). The extended marginal zone straddles the current
 368 grounding zone (see Fig. 5a) while the majority of the anti-flow line is dozens of kilometers
 369 away.

How?

Opposite typical topo control

How fast?

Slow creep expected on rock?

4.2 Overburden could account for spatial variations in sediment strength

Basal conditions along the anti-flow line A-A' vary significantly due to variations in basal topography, lithology and hydrology [Siegert *et al.*, 2016]. Out of the three contributors to varying basal conditions, the structure and properties of the subglacial drainage network are particularly difficult to constrain observationally. Theoretically, many different configurations are possible [e.g., Flowers, 2015], but not all of them will result in basal strength profiles that are compatible with surface velocities [Rignot *et al.*, 2011].

Figure 6 focuses on better constraining variations in basal strength in the sediment portion of the bed. It shows the two simulations for which computed surface speeds provide the best fit to observed surface speeds (Figs. 6a1 and b1) and transverse strain rates (Figs. 6a2 and b2) when assuming constant (Figs. 6a1-a4) or linearly varying (Figs. 6b1-b4) basal conditions. In both cases, we assume that the lithologic transition from rock to sediments occurs in the vicinity of the western shear margin as highlighted in Figures 6a3 and b3, where the rock portion of the domain is shown in blue and the till portion in red, respectively. For all simulations, we assume impose a similarly sharp increase in till strength outside of the Eastern shear margin, which could either represent a transition from temperate to frozen as hypothesized by Siegert *et al.* [2016] or a transition from wet to dry sediments.

Our simulations demonstrate that the assumed basal strength profile dominates not only the computed surface speeds in Figures 6a1 and b1, but also the englacial temperature distribution shown in Figures 6a4 and b4. In Figures 6a1-a4, the sediment-portion of the bed is relatively weak and the rock-portion of the bed plays a more important role in the overall force balance as compared to Figures 6b1-b4, where the sediment strength increases towards the western shear margin. As a consequence, shear heating is concentrated in the western shear margin in Figures 6a1-a4, where the bed transitions from relatively weak sediments to hard rock with a reasonable but high sliding coefficient. In Figures 6b1-b4, shear heating is concentrated in the eastern shear margin, where the sediment strength is lowest but rapidly increasing towards the ridge. Our simulations suggest that an abrupt transition between weak and strong sediments is necessary to reproduce the high strain rates of the eastern shear margin (see Figs. 6b2). Overall, the sediment-dominated portion of the bed plays a more important role in the force balance in the latter case (Figs. 6b1-b4).

We find that the best fitting sediment strength is a linearly decreasing profile from the to the eastern shear margin (Figs. 6b1-b4). The best fitting strength profile varies linearly

of considered

402 from 29.85 to 18.35 kPa across the ice stream trunk. Our inferred variation of basal strength
 403 mimics the approximately linear basal topography across the trunk. The ice thickness across
 404 the ice stream trunk varies from approximately 1700 to 1000 meters, modifying the overbur-
 405 den pressure on the underlying hydrological system. The basal strength, τ_c , is a function of
 406 the pore pressure at the sliding interface, p , through

$$\tau_c = f(\rho g H - p) + c = f \rho g H(1 - k_p) + c, \quad (22)$$

407 with friction parameter, $f \approx 0.5 - 0.6$ [Rathbun *et al.*, 2008], sediment cohesion, $c \approx 1 - 2$
 408 kPa [Kamb, 2001], and flotation fraction, k_p , which varies from 0 (no-flotation) to 1 (full
 409 flotation). Considering the linear ice thickness profile from 1700 to 1000 meters, we find that
 410 the slope in basal strength suggested by Figs. 6b1-b4 mimics the slope at which ice thickness
 411 increases in the domain. Assuming a constant average flotation factor of $k_p = 0.996$ in the
 412 entire sediment-portion of the domain recovers a linear profile from approximately 31 to 19
 413 kPa. This variation is consistent with the best-fitting basal strength profile shown in Figure 6.

414 Our result that the gradient in best-fitting basal strength mimics the overburden sug-
 415 gests that the simplest possible hydrological system is a spatially well-connected drainage
 416 network near flotation. Needless to say, there might be considerable small-scale variability
 417 not resolved here. There might also be additional large-scale variations that either correlate
 418 with or follow a similar trend as the overburden stress and are hence difficult to differenti-
 419 ate from ice-thickness effects. We merely note here that it is not necessary to invoke this
 420 complexity in most of the domain for the model to be compatible with surface observables
 421 (Fig. 6b1). That being said, we implicitly assume small-scale variability in the subglacial
 422 drainage system when enforcing an increase in basal strength at the eastern shear margin.
 423 The best fitting simulation shown in Figures 6b1-b4 entails a temperate zone in the east-
 424 ern shear margin that could potentially feed a meltwater channel in the margin as has been
 425 suggested for the Siple Coast [Perol and Rice, 2015; Platt *et al.*, 2016; Suckale *et al.*, 2014;
 426 Elsworth and Suckale, 2016a]. Alternatively, the increase in bed strength could result from
 427 freezing [Schoof, 2004, 2012; Suckale *et al.*, 2014; Perol *et al.*, 2015; Haseloff *et al.*, 2015].
 428 The latter explanation would require lateral advection of cold ice into the eastern shear mar-
 429 gin to counteract the heating entailed in the measured strain rates (Figs. 6b2) and an addi-
 430 tional englacial process like fabric to explain the narrow margin width.

overburden
 w/ const k_p
 well connected?
 may be uniform?
 seems weak?
 advection?
 fabric?
 can
 shear?
 happen?

4.3 Drainage dominates sliding over hard rock

431 While Figure 6b1 fits the measured anti-plane speed well for the eastern shear margin
 432 and the majority of the ice-stream trunk, it captures the behavior of the western shear margin
 433 and extended marginal zone less well. The MEASUREs data shown in Fig. 6b1 indicates
 434 more spatial variability than the model solution entails. One potential explanation is that the
 435 velocity-strengthening sliding law [Weertman, 1957] with spatially constant sliding coeffi-
 436 cient in Fig. 6 is questionable for hard-rock sliding in the presence of pervasive subglacial
 437 water [Lliboutry, 1968; Iken, 1981; Fowler, 1986, 1987; Schoof, 2005; Gagliardini *et al.*,
 438 2007], particularly in light of the high pore pressures we infer for the sediment-dominated
 439 portion of the model domain. Including cavitation has the effect that the bed strength reaches
 440 a finite value after which it remains approximately constant or even declines with faster flow
 441 [Iken, 1981; Schoof, 2005; Gagliardini *et al.*, 2007]. We capture regularized Coulomb slid-
 442 ing by assuming that the entire bed behaves plastically.
 443

444 In Figure 7, we test whether a plastic bed with variable strength improves the fit to ob-
 445 served surface speeds in the western shear margin and extended marginal zone. Similarly
 446 to Figure 6, we restrict our tests to constant and linearly varying basal strength profiles. To
 447 highlight that regularized Coulomb sliding is equivalent to plastic behavior of the bed, we
 448 plot both the hard-rock and the sediment-dominated portion of the domain in red in Fig-
 449 ure 7a3 and b3. Building on our analysis from Figure 6, we assume that the basal strength
 450 of the sediments decreases linearly from the western to the eastern shear margin.

451 The two best fitting simulations shown in Figure 7 demonstrate that switching the na-
 452 ture of sliding does not improve the fit to observed surface speed and strain rates. When as-
 453 suming a constant basal strength, we are unable to reproduce the slow but finite sliding out-
 454 side of the western shear margin (see Fig. 7a1). In comparison, velocity-strengthening slid-
 455 ing (see Fig. 6) is consistent with the observed slow slip. A linearly increase basal strength
 456 profile provides a better fit in the extended marginal zone, but fails to capture the western
 457 shear margin (see Fig. 7b1 and b2). We emphasize that, contrary to Figure 6, it is not clear
 458 why the basal strength in the extended marginal zone would increase linearly, because over-
 459 burden is approximately constant in the extended marginal zone.

460 A missing component in our modeling of subglacial conditions so far is the presence
 461 of the meltwater channel that emanates from underneath the western shear margin at the
 462 grounding line (see Fig. 1a). The precise location of the meltwater channel is only known

Is this strong enough?

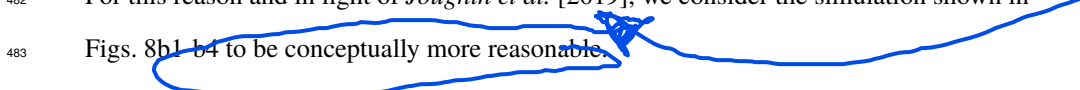
Not quite true.

Is this well justified?
why not a fan flow?

No clear reason

for the ice shelf [Alley *et al.*, 2016]. We assume that it follows the trough in basal topography that delineates the main trunk of Institute in the vicinity of the western shear margin. The meltwater channel locally strengthens the bed, because it provides more efficient drainage than thin-film flow, leaving the adjacent bed relatively water-poor [Hewitt, 2011; Perol *et al.*, 2015; Elsworth and Suckale, 2016a]. Little is known about how fast the pressure perturbation induced by a meltwater channel decays spatially in the presence of both lithological and topographic variations. For a plastic bed, we assume a constant decay rate, γ , everywhere, implying that the channel alters bed strength similarly irrespective of lithology and local topography.

In Figure 8, we analyze how a channel underneath the western shear margin could alter bed strength and surface observables for classical sliding (Figs. 8a1-a4) and regularized Coulomb sliding (Figs. 8b1-b4). In the sediment-dominated portion of the domain, we superimpose the basal strengthening of the channel with a linear decrease in bed strength towards the eastern shear margin as a result of decreasing overburden (see Fig. 6). The agreement between measured surface speed (Figs. 8a1,b1) and strain rate (Figs. 8a2,b2), improves significantly as compared to Fig. 7. Relatively to each other, the quality of fit is comparable when assuming a linear increase in the sliding coefficient towards the channel (Figs. 8a3). We highlight that it is unknown if and how the sliding coefficient β might vary in the vicinity of a subglacial channel. It is hence not clear that a linearly varying basal strength is justified. For this reason and in light of Jougin *et al.* [2019], we consider the simulation shown in Figs. 8b1-b4 to be conceptually more reasonable.



What from it?

Figure 8 suggests that the basal strength distribution over the hard-rock bed is dominated by the existence of a meltwater channel in or close to the shear margin. Simpler strength distributions in the extended marginal zone (e.g., Figure 7) are not compatible with surface observables. In contrast, Figure 6 demonstrates that the presence of a channel is not a necessary component for obtaining a satisfactory fit to surface speed and strain rates in the sediment-dominated portion of the domain. One possibility is that the channel does not affect the western and eastern portions of the bed equally as we have assumed here in the interest of simplicity, which is conceivable in light of the asymmetries in both topography and lithology around that location. In fact, the hydrological model by Perol *et al.* [2015] suggests that the spatial reach of the channel-induced pressure perturbation on a flat bed is likely smaller than assumed here.

4.4 Potential dynamic consequence of increased melting at the grounding zone

The finding that channelized drainage in the western shear margin plays an important role in the overall force balance at Institute suggests that changes in the subglacial hydrology could sensitively affect ice dynamics. At Institute, changes in the hydrology are expected to arise at or in the vicinity of the grounding zone, where a redirection of coastal currents could cause increased transport of warm water into the subsurface ice cavity [Hellmer *et al.*, 2012]. On decadal time scales, the consequence could be ice-shelf collapse and unstable retreat of Institute Ice Stream. Here, we quantify a potentially more immediate impact of increased melt rates at the grounding line on ice-stream dynamics that results from warm ocean waters carving into the meltwater channel underneath the western shear margin (see Fig. 1).

The pressure and drainage rate in a Röhlisberger channel is closely connected to its cross-sectional diameter. At steady-state, the diameter of the channel represents the balance of turbulent dissipation in the water widening the channel and viscous creep from the ice closing it [Röhlisberger, 1972]. We assume that warm ocean waters in the subsurface cavity carve into the channel at the grounding line, widening the channel diameter slightly beyond its steady-state shape and thereby reducing the pressure gradient. We emphasize that the interactions between the hydrological system underneath grounded ice and oceanic subcavity flow is incompletely understood. However, pronounced channel features documented at the surface of several Antarctic ice shelves [LeBrocq *et al.*, 2013], some of which are hundreds of meters in width, lend support to the idea that subglacial channels may widen upon interaction with the ocean.

Figure 9 shows the dynamic consequences of reducing the basal strengthening induced by the channel by approximately 3% for the two cases shown in Figure 8. Panel 9A assumes classical, velocity-strengthening sliding on hard rock with the variability in basal strength and sliding coefficient shown in Figures 8a1-a4. The simulations in panel 9B are based on an entirely plastic bed with a meltwater channel underneath the western shear margin dominating basal strength and corresponds to Figures 8b1-b4. The impact of changes in the efficiency of meltwater drainage on ice-stream dynamics are significantly more pronounced for an entirely plastic bed (Fig. 9B).

Our simulations suggest that in the case of regularized Coulomb sliding, speed-up of the ice stream occurs to a similar degree everywhere in the model domain, despite the localized change in the drainage of only the meltwater channel. Stress transmission in the ice col-

*think about
shelves more
water
creeping
up R-channels?
Is this seen?
how far upstream?*

*B/c non-local
control in
plastic case.*

umn over the weak bed propagates more than 50 ice thicknesses across the ice stream. Classical hardrock sliding suppresses a similarly dynamic response, with only a slight increase in surface speed in the main portion of the trunk.

The fact that changes in basal conditions manifest non-locally in the shear margins is an important consideration for interpretation and organization of field measurements. This analysis motivates fieldwork that maintains a system-level view of data across an ice stream in order to quantify the effect of stress partitioning between margins, shown in Figure 9b. Our analysis shows that simultaneous instrumentation of Institute's shear margins and observations of coupled migration rates is likely necessary to inform future evolution of the drainage basin.

5 Discussion

We develop a generalized anti-flow line model for analyzing the cross-sectional stability of ice streams and apply the model to Institute Ice Stream. Our work is motivated jointly by the advances that simplified models have made to our understanding of the role of shear margins in ice-stream dynamics [Jacobson and Raymond, 1998; Schoof, 2004, 2012; Suckale *et al.*, 2014; Haseloff *et al.*, 2015; Perol *et al.*, 2015; Perol and Rice, 2015; Platt *et al.*, 2016; Elsworth and Suckale, 2016a] and by the increasing resolution of remotely-sensed data probing the ice sheets in unprecedented detail [Schroeder *et al.*, 2014; Siegert *et al.*, 2016; Muto *et al.*, 2019; Koellner *et al.*, 2019]. To be able to analyze both speed-up and changes in the extent of the basal slip zone, we develop a thermomechanical free-boundary formulation building on Schoof [2006b] that does not require *a priori* knowledge of shear-margin positions.

The main contribution of our model approach is to integrate thermomechanical effects into the original formulation by Schoof [2006b] and leveraging the computational advances of the Disciplined Convex Optimization framework by Grant and Boyd [2008]. Our model captures topographic variability in the model domain and allows for different boundary conditions based on variable subglacial lithology and hydrology. Including these complexities means that a simple cross-section perpendicular to the main flow direction does not generally abide by the anti-plane shear assumption on which models for shear margins [Jacobson and Raymond, 1998; Schoof, 2004, 2012; Suckale *et al.*, 2014; Haseloff *et al.*, 2015; Perol *et al.*, 2015; Platt *et al.*, 2016; Elsworth and Suckale, 2016a] rely. Instead, we develop an

Motivate the error terms? May I
error in each approach?

584 algorithm to compute the appropriate anti-flow lines for a given field site from measured sur-
 585 face data [Rignot *et al.*, 2011]. Anti-flow lines capture the locations that contribute to the
 586 cross-sectional force balance of the ice stream.

587 We apply our model to Institute Ice Stream, which has attracted attention in recent year
 588 because of its dynamic history [Siegert *et al.*, 2013; Winter *et al.*, 2015] and the potential
 589 for future destabilization through increased melt rates in response to projected shifts of the
 590 coastal current into the Filchner-Ronne Ice Shelf [Hellmer *et al.*, 2012]. One consequence on
 591 the time scale of several decades or even centuries could be ice shelf collapse and the onset
 592 of the Marine Ice Sheet Instability Wright *et al.* [2014]. However, as pointed out by Siegert
 593 *et al.* [2016], changes in ice-stream dynamics are also important for assessing Institutes fu-
 594 ture stability. Extensive airborne geophysical surveys by the British Antarctic Survey [Jordan
 595 *et al.*, 2013; Siegfried *et al.*, 2016] have provided the necessary observational constraints and
 596 we leverage some of this data here to improve our process-based understanding of the sub-
 597 glacial conditions and overall stability of Institute.

598 We focus on modeling the radar profile of Siegert *et al.* [2016] that is most perpen-
 599 dicular to flow and compute the corresponding anti-flow line from InSAR-derived surface
 600 velocity data by Rignot *et al.* [2011]. While the anti-flow line is approximately perpendicular
 601 to the main flow direction in the main trunk of Institute, it curves around to an almost parallel
 602 alignment in the slowly slipping ridge to the West of the main trunk (see Fig. 5. While seem-
 603 ingly an area that would contribute little to the overall stability of Institute due to its slow
 604 slip speed, we suggest that it could be very relevant dynamically, because it couples stress
 605 changes in the vicinity of the grounding line to the main trunk of Institute Ice Stream.

606 Our simulations show that the future stability of Institute depends sensitively on whether
 607 slip in the hard-rock portion of the domain occurs through regularized Coulomb sliding [Iken,
 608 1981; Schoof, 2005; Gagliardini *et al.*, 2007] or through classical, velocity-strengthening
 609 sliding [Weertman, 1957; Iverson and Zoet, 2015] as illustrated in Figure 9. We note that
 610 regularized Coulomb sliding is conceptually more appropriate in the context of our field set-
 611 ting, which appears to be characterized by high basal water pressures and proximity of the
 612 grounding line (see Fig. 1). It is also supported by recent evidence that the observed eleva-
 613 tion and speed-up of Pine Island Glacier, Antarctica, is indicative of regularized Coulomb
 614 sliding [Joughin *et al.*, 2019].

The main contributor to the spatial variability of bed strength along the A-A' anti-flow line at Institute is the presence of a meltwater channel emanating approximately from underneath the western shear margin (see Fig. 1). Contrary to other channels that have been inferred to exist under some of the ice streams in the Siple Coast [Suckale *et al.*, 2014; Perol *et al.*, 2015; Perol and Rice, 2015; Platt *et al.*, 2016; Elsworth and Suckale, 2016b], the channel is not associated with a temperate zone in the western margin. Instead, it appears to be fed by upstream and potentially lateral water influx from the eastern shear margin [Siegert *et al.*, 2016]. The presence of the channel masks the lithological transition from hard rock to sediment in its vicinity. Our simulations hence indicate that the stability of the western shear margin may still be controlled primarily by hydrology, despite variations in lithology and topography in its vicinity. Contrary to other shear margins that may be hydrological controlled [Perol *et al.*, 2015; Perol and Rice, 2015; Elsworth and Suckale, 2016b], it is unlike to migrate, because the position of the channel at Institute is topographically controlled.

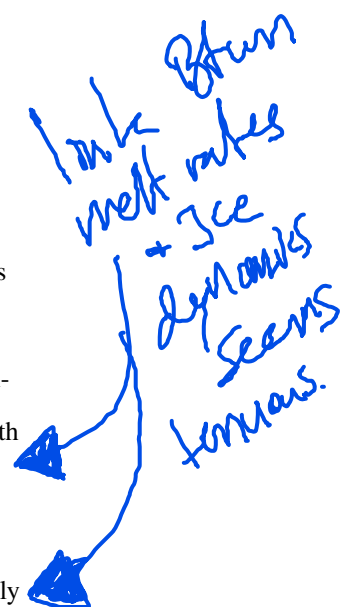
An important uncertainty in assessing the future stability of Institute Ice Stream is the behavior of the eastern shear margin. An abrupt transition between weak and strong sediments at this location is necessary to match surface velocity data. In the absence of additional observational constraints, it is not possible to conclusively determine the physical mechanism locking the eastern shear margin at Institute. The two main possibilities are a frozen to thawed transition [Schoof, 2012; Haseloff *et al.*, 2015] or hydrological processes [Perol *et al.*, 2015; Perol and Rice, 2015; Elsworth and Suckale, 2016b] as have been inferred for the downstream portion of Bindschadler and Kamb Ice Streams. In the margin of Bindschadler, both hydrological pathways and ice shelf signatures of channelized drainage [Le-Brocq *et al.*, 2013; Alley *et al.*, 2018] pointed to the potential existence of an efficient drainage element [Elsworth and Suckale, 2016a]. However, Institute does not exhibit similar evidence of meltwater collection in the Eastern margin [LeBrock *et al.*, 2013; Alley *et al.*, 2018] and hydrologic potential diverts flow away from the margin.

Our study emphasizes the need to understand the diversity of shear margins across the ice sheet, and the variety of physical processes that govern them. Physical mechanisms include thermal [Schoof, 2004, 2012; Suckale *et al.*, 2014; Haseloff *et al.*, 2015], hydrological [Perol *et al.*, 2015; Perol and Rice, 2015; Platt *et al.*, 2016; Elsworth and Suckale, 2016a; Minchew *et al.*, 2018], fabric [Minchew *et al.*, 2018], topographic [Stearns *et al.*, 2008], and lithologic [Winsborrow *et al.*, 2010] controls on shear margin position and stability. All shear margins will exhibit some combination of each of these controls. Finding natural laborato-

648 tries for quantifying their relative importance and mutual interdependence enables a better
 649 understanding of shear-margin stability in complex settings. Of particular relevance for these
 650 studies is the Eastern shear margin of Thwaites Glacier, where the lateral extent of ice flow
 651 is poorly understood [Macgregor *et al.*, 2013; Schroeder *et al.*, 2013]. Through a targeted
 652 understanding of the underlying processes governing shear margins we can hope to better
 653 inform future projections of fast ice flow across the ice sheets.

654 6 Conclusions

655 Our study is motivated by the need to apply process-based models of shear-margin
 656 stability to field sites that inevitably exhibit much more complexity than current, idealized
 657 models capture. We propose a thermomechanical anti-plane-flow line model that quantifies
 658 the joint effect of variable topography, lithology and hydrology on large-scale ice motion.
 659 We verify and benchmark this model against solutions of Schoof [2006a] and apply it to In-
 660 stitute Ice Stream in West Antarctica. We find that the basal strength distribution underneath
 661 Institute Ice Stream appears to be controlled primarily by hydrological process despite the
 662 compounding effects of lithology and topography. This finding suggests that the projected
 663 increase of melt rates in the Weddell Sea Sector could affect ice-stream dynamics sensitively
 664 even prior to the onset of grounding line retreat, highlighting that Institute might be vulne-
 665 rable to ocean forcing than large-scale ice-sheet models suggest.



666 A: Variational Formulation of the Mechanical Model

Cases of negative velocities, $\tau_c < 0$, are excluded following the stability and uniqueness analysis of Schoof [2006a]. We consider two regions of the basal boundary; regions with sliding or failure ($u > 0$), Γ_f , and regions that are locked ($u = 0$), Γ_r . Basal boundary conditions then become

$$-\eta|\nabla u|^{1/n-1}u_n = \tau_b \quad \text{if } u > 0 \quad (\text{A.1})$$

$$-\eta|\nabla u|^{1/n-1}u_n \leq \tau_b \quad \text{if } u = 0 \quad \text{on } \Gamma_{\text{bed}}. \quad (\text{A.2})$$

A variational formulation allows us to formulate this problem, such that substrate failure occurs consistently with global force balance, providing a self-consistent determination of locked and failing basal conditions. Transitioning to this formulation will not explicitly require the locations of Γ_f and Γ_r . Assuming a suitable test function, v , we construct the

671 variational formulation as,

$$\int_{\Omega} \rho g \sin \alpha(v - u) = \int_{\Omega} \eta |\nabla u|^{1/n-1} \nabla u \cdot \nabla(v - u) - \int_{\partial\Omega} \eta |\nabla u|^{1/n-1} u_n (v - u), \quad (\text{A.3})$$

672 and applying the boundary conditions,

$$0 = \int_{\Omega} \eta |\nabla u|^{1/n-1} \nabla u \cdot \nabla(v - u) - \int_{\Omega} \rho g \sin \alpha(v - u) + \int_{\Gamma_f} \tau_b (v - u) + \int_{\Gamma_r} (-\eta |\nabla u|^{1/n-1} u_n) v, \quad (\text{A.4})$$

673 on the failing ($u > 0$), Γ_f , and locked ($u = 0$), Γ_r , boundaries.

674 With the assumption of positive velocities, it follows that $-\eta |\nabla u|^{1/n-1} u_n v \leq \tau_b |v| =$
 675 $\tau_b (|v| - |u|)$ on Γ_r , and $\tau_b (v - u) \leq \tau_b (|v| - |u|)$ on Γ_f . This simplifies the variational
 676 inequality,

$$0 \leq \int_{\Omega} \eta |\nabla u|^{1/n-1} \nabla u \cdot \nabla(v - u) + \int_{\Gamma} \tau_b (|v| - |u|) - \int_{\Omega} \rho g \sin \alpha(v - u). \quad (\text{A.5})$$

677 that considers the entire boundary, Γ , without explicitly distinguishing failing and locked
 678 portions.

Following Schoof [2006a] and letting $p = 1 + 1/n$, we can define an energy on v .

Solving Equation (11) then becomes equivalent to the optimization problem

$$\text{minimize} \quad J(v) = \frac{1}{p} \int_{\Omega} \eta |\nabla v|^p + \int_{\Gamma} \tau_b |v| - \int_{\Omega} \rho g \sin \alpha v \quad (\text{A.6})$$

$$\text{subject to} \quad v \geq 0. \quad (\text{A.7})$$

679 This energy, $J(v)$, has been proven to be convex in $v \geq 0$, and unique when a solution ex-
 680 ists [Schoof, 2006a].

681 B: Transforming Mechanical Energy Functional to DCP Framework

To demonstrate how the problem can be reformulated to be amenable to the CVX algorithm, each of the terms in the energy functional must be decomposed into the composition of convex operators. Define each term in the energy functional described by Equation 17 as,

$$J(v_i) = J_A(v_i) + J_B(v_i) + J_C(v_i). \quad (\text{B.1})$$

For example, the $J_A(v_i)$ on a single element, τ , becomes,

$$J_A(v_i) = \frac{1}{p} \eta \int_{\tau} \left| \sum_{i=1}^3 v_i \nabla \phi_i \right|^p \quad (\text{B.2})$$

$$= \frac{1}{p} \eta d\tau \left\| \begin{bmatrix} \mathbf{D}_x \mathbf{v}_{\tau} \\ \mathbf{D}_y \mathbf{v}_{\tau} \end{bmatrix} \right\|^p, \quad (\text{B.3})$$

with discretized gradient operators, \mathbf{D}_x and \mathbf{D}_y , and strictly positive element area, $d\tau$. The discretized gradient operations are affine functions on element velocities, \mathbf{v}_τ , which are convex. The norm operation is convex, followed by the power operation, which is convex for $p > 1$. Multiplication with strictly positive coefficients demonstrates that $J_A(v_i)$ is convex.

Similarly, we decompose $J_B(v_i)$ on a single boundary edge, γ ,

$$J_B(v_i) = \sum_{i=1}^2 v_i \int_\gamma \tau_b(v) \phi_i \quad (\text{B.4})$$

$$= \sum_{i=1}^2 v_i \int_\gamma \tau_b(v_i) \quad (\text{B.5})$$

$$= \sum_{i=1}^2 v_i d\gamma \tau_b(v_i) \quad (\text{B.6})$$

$$= d\gamma \boldsymbol{\tau}_b(\mathbf{v}_\gamma)^T \mathbf{v}_\gamma, \quad (\text{B.7})$$

with nodal basal tractions, $\tau_b(v_i)$, and boundary edge length, $d\gamma$. $J_B(v_i)$ is convex on edge velocities, \mathbf{v}_γ , for basal tractions, $\tau_b(v) = |v|^m$ only when $m > 0$. This means that $J_B(v_i)$ remains convex only when the sliding law is perfectly-plastic, $m = 0$, or velocity strengthening, $m > 0$, but not the unstable case of a velocity weakening sliding law, $m < 0$.

Finally, $J_C(v_i)$ on a single element, τ , becomes,

$$J_C(v_i) = -\rho g \sin \alpha \sum_{i=1}^3 v_i \int_\tau \phi_i \quad (\text{B.8})$$

$$= -f d\tau \mathbf{1}^T \mathbf{v}_\tau, \quad (\text{B.9})$$

with driving stress, $f = \rho g \sin \alpha$. $J_C(v_i)$ is an affine function on element velocities, \mathbf{v}_τ , and is therefore convex.

The summation of convex functions is convex, proving that the fully-discretized energy functional (i.e. the summation of each of these terms over all elements and boundary edges) is convex in v . Simplifying and vectorizing, the fully-discretized energy becomes,

$$J(\mathbf{v}) = \frac{1}{p} \eta \mathbf{d}\boldsymbol{\tau}^T \|[\mathbf{D}_x \mathbf{v}, \mathbf{D}_y \mathbf{v}]\|^p + (\mathbf{d}\boldsymbol{\gamma} \circ \boldsymbol{\tau}_b)^T \mathbf{v}_b - (\mathbf{d}\boldsymbol{\tau} \circ \mathbf{f})^T \mathbf{v}, \quad (\text{B.10})$$

with elementwise multiplication, \circ , boundary nodal values, \cdot_b , and second-dimension vectorwise norm, $\|\cdot\|$. Therefore, the fully-discretized energy functional is a convex function on the vectorized velocity, \mathbf{v} .

698 **Acknowledgments**

699 This research was supported by the National Science Foundation through the Office of Po-
 700 lar Programs awards PLR-1341499, PLR-1744758, and PLR-1739027. The authors thank
 701 Dustin Schroeder, Neal Iverson, Luke Zoet, Knut Christianson, and Mark Fahnestock for
 702 fruitful discussions. The authors also thank two anonymous reviewers for their comments
 703 that greatly improved the manuscript. Observational data including MEaSUREs surface ve-
 704 locity measurements and locations of subglacially-sourced channels are publicly available
 705 through the National Snow & Ice Data Center (<https://nsidc.org/data/>). This code devel-
 706 oped in this paper is available open-source under the GNU General Public License, version
 707 3 on the SIGMA research group (SImulations of Geophysical Multi-phAse flows) webpage
 708 (<https://pangea.stanford.edu/researchgroups/sigma/sigmagitlab>).

709 **References**

- 710 ()
- 711 Alley, K. E., T. A. Scambos, M. R. Siegfried, and H. A. Fricker (2016), Impacts of warm
 712 water on Antarctic ice shelf stability through basal channel formation, *Nature Geoscience*,
 713 (March), doi:10.1038/ngeo2675.
- 714 Alley, K. E., T. A. Scambos, A. R. S., H. Rajaram, A. Pope, and T. M. Haran (2018),
 715 Continent-wide estimates of Antarctic strain rates from Landsat 8-derived velocity grids,
 716 *Journal of Glaciology*, pp. 1–12, doi:10.1017/jog.2018.23.
- 717 Bamber, J. L., D. G. Vaughan, and I. Joughin (2000), Widespread complex flow in the inte-
 718 rior of the Antarctic ice sheet, *Science*, 287(5456), 1248–1250.
- 719 Bingham, R. G., and M. J. Siegert (2007), Radar-derived bed roughness characterization of
 720 Institute and Möller ice streams, West Antarctica, and comparison with Siple Coast ice
 721 streams, *Geophysical Research Letters*, 34(21), 1–5, doi:10.1029/2007GL031483.
- 722 Brenner, S., and R. Scott (2007), *The mathematical theory of finite element methods*, vol. 15,
 723 Springer Science & Business Media.
- 724 Elsworth, C. W., and J. Suckale (2016a), Rapid ice flow rearrangement induced by sub-
 725 glacial drainage in West Antarctica, *Geophysical Research Letters*, 43, 11,697–11,707,
 726 doi:10.1002/2016GL070430.
- 727 Elsworth, C. W., and J. Suckale (2016b), Subglacial drainage induces rapid ice flow rear-
 728 rangement in West Antarctica, *Proceedings of the National Academy of Sciences*, submit-
 729 ted, doi:10.1073/pnas.xxxxxxxxxxx.

- 730 Flowers, G. E. (2015), Modelling water flow under glaciers and ice sheets, *Proceedings of*
731 *the Royal Society A*, 471.
- 732 Fowler, A. (1986), A sliding law for glaciers of constant viscosity in the presence of sub-
733 glacial cavitation, *Proceedings of the Royal Society of London. A. Mathematical and Phys-*
734 *ical Sciences*, 407(1832), 147–170.
- 735 Fowler, A. (1987), Sliding with cavity formation, *Journal of Glaciology*, 33(115), 255–267.
- 736 Friedman, A. (2010), *Variational principles and free-boundary problems*, Courier Corpora-
737 tion.
- 738 Gagliardini, O., D. Cohen, P. Råback, and T. Zwinger (2007), Finite-element modeling of
739 subglacial cavities and related friction law, *Journal of Geophysical Research: Earth Sur-*
740 *face*, 112(F2).
- 741 Glen, J. W. (1955), The creep of polycrystalline ice, *Proceedings of the Royal Society of Lon-*
742 *don A: Mathematical, Physical and Engineering Sciences*, 228(1175).
- 743 Grant, M., and S. Boyd (2008), Graph implementations for nonsmooth convex programs, in
744 *Recent Advances in Learning and Control*, edited by V. Blondel, S. Boyd, and H. Kimura,
745 Lecture Notes in Control and Information Sciences, pp. 95–110, Springer-Verlag Limited.
- 746 Grant, M., and S. Boyd (2013), {CVX}: Matlab Software for Disciplined Convex Program-
747 ming, version 2.1, \url{http://cvxr.com/cvx}.
- 748 Greene, C. A., D. E. Gwyther, and D. D. Blankenship (2017), Antarctic Mapping Tools for
749 MATLAB, *Computers and Geosciences*, 104, 151–157, doi:10.1016/j.cageo.2016.08.003.
- 750 Haseloff, M., C. Schoof, and O. Gagliardini (2015), A boundary layer model for ice stream
751 margins, *Journal of Fluid Mechanics*, 781, 353–387, doi:10.1017/jfm.2015.503.
- 752 Hellmer, H. H., F. Kauker, R. Timmermann, J. Determann, and J. Rae (2012), Twenty-first-
753 century warming of a large antarctic ice-shelf cavity by a redirected coastal current, *Na-*
754 *ture*, 485(7397), 225.
- 755 Hewitt, I. J. (2011), Modelling distributed and channelized subglacial drainage:
756 the spacing of channels, *Journal of Glaciology*, 57(202), 302–314, doi:
757 10.3189/002214311796405951.
- 758 Hooke, R. L., C. F. Raymond, R. L. Hotchkiss, and R. J. Gustafson (1979), Calculations of
759 velocity and temperature in a polar glacier using the finite-element method, *Journal of*
760 *Glaciology*, 24(90), 131–146.
- 761 Iken, A. (1981), The effect of the subglacial water pressure on the sliding velocity of a
762 glacier in an idealized numerical model, *Journal of Glaciology*, 27(97), 407–421.

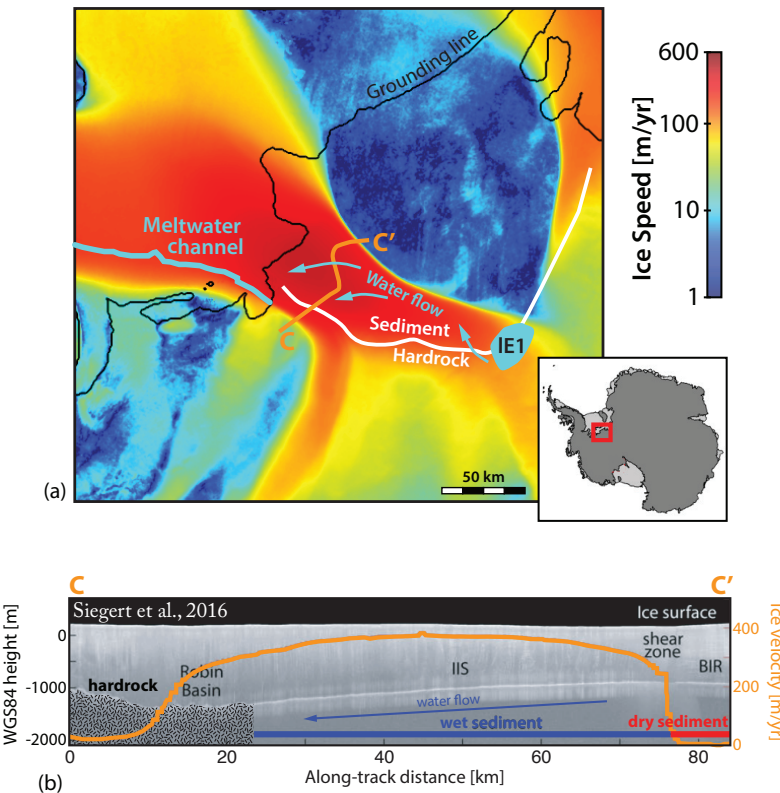
- Iverson, N. R., and L. K. Zoet (2015), Experiments on the dynamics and sedimentary products of glacier slip, *Geomorphology*, 244, 121–134, doi:10.1016/j.geomorph.2015.03.027.
- Jacobson, H. P., and C. F. Raymond (1998), Thermal effects on the location of ice stream margins, *Journal of Geophysical Research*, 103(12), 111–122.
- Jamieson, S. S. R., A. Vieli, S. J. Livingstone, C. Ó. Cofaigh, C. Stokes, C.-D. Hillenbrand, and J. a. Dowdeswell (2012), Ice-stream stability on a reverse bed slope, *Nature Geoscience*, 5(11), 799–802, doi:10.1038/ngeo1600.
- Jordan, T. A., F. Ferraccioli, N. Ross, H. F. Corr, P. T. Leat, R. G. Bingham, D. M. Rippin, A. le Brocq, and M. J. Siegert (2013), Inland extent of the Weddell Sea Rift imaged by new aerogeophysical data, *Tectonophysics*, 585, 137–160, doi:10.1016/j.tecto.2012.09.010.
- Joughin, I., B. E. Smith, and B. Medley (2014), Marine Ice Sheet Collapse Potentially Under Way for the Thwaites Glacier Basin, West Antarctica, *Science*, 344(May), 735–739.
- Joughin, I., B. E. Smith, and C. G. Schoof (2019), Regularized coulomb friction laws for ice sheet sliding: Application to pine island glacier, antarctica, *Geophysical Research Letters*, 46(9), 4764–4771.
- Kamb, B. (2001), Basal Zone of the West Antarctic Ice Streams and its Role in Lubrication of Their Rapid Motion, *The West Antarctic Ice Sheet: Behavior and . . .*, 77, 157–199.
- Koellner, S., B. Parizek, R. Alley, A. Muto, N. Holschuh, and S. Nowicki (2019), The impact of spatially-variable basal properties on outlet glacier flow, *Earth and Planetary Science Letters*, 515, 200–208, doi:10.1016/j.epsl.2019.03.026.
- LeBrocq, A. M., N. Ross, J. A. Griggs, R. G. Bingham, H. F. J. Corr, F. Ferraccioli, A. Jenkins, T. A. Jordan, A. J. Payne, D. M. Rippin, and M. J. Siegert (2013), Evidence from ice shelves for channelized meltwater flow beneath the Antarctic Ice Sheet, *Nature Geoscience*, 6(November), 945–948, doi:10.1038/ngeo1977.
- Lliboutry, L. (1968), General theory of subglacial cavitation and sliding of temperate glaciers, *Journal of Glaciology*, 7(49), 21–58.
- Macgregor, J. A., G. A. Catania, H. Conway, D. M. Schroeder, I. Joughin, D. A. Young, S. D. Kempf, and D. D. Blankenship (2013), Weak bed control of the eastern shear margin of Thwaites Glacier, West Antarctica, *Journal of Glaciology*, 59(217), 900–912, doi:10.3189/2013JoG13J050.
- Meyer, C. R., and B. M. Minchew (2018), Temperate ice in the shear margins of the Antarctic Ice Sheet: Controlling processes and preliminary locations, *Earth and Planetary Science Letters*, 498, 17–26, doi:10.1016/j.epsl.2018.06.028.

- 796 Milillo, P., E. Rignot, P. Rizzoli, B. Scheuchl, J. Mouginot, J. Bueso-Bello, and P. Prats-
797 Iraola (2019), Heterogeneous retreat and ice melt of thwaites glacier, west antarctica, *Sci-
798 ence advances*, 5(1), eaau3433.
- 799 Minchew, B. M., C. R. Meyer, A. A. Robel, G. H. Gudmundsson, and M. Simons (2018),
800 Processes controlling the downstream evolution of ice rheology in glacier shear margins:
801 case study on Rutford Ice Stream, West Antarctica, *Journal of Glaciology*, 64(246), 583–
802 594, doi:10.1017/jog.2018.47.
- 803 Muto, A., S. Anandakrishnan, R. B. Alley, H. J. Horgan, B. R. Parizek, S. Koellner,
804 K. Christianson, and N. Holschuh (2019), Relating bed character and subglacial morphol-
805 ogy using seismic data from Thwaites Glacier, West Antarctica, *Earth and Planetary Sci-
806ence Letters*, 507, 199–206, doi:10.1016/j.epsl.2018.12.008.
- 807 Perol, T., and J. R. Rice (2015), Shear heating and weakening of the margins of
808 West Antarctic ice streams, *Geophysical Research Letters*, 42(9), 3406–3413, doi:
809 10.1002/2015GL063638.
- 810 Perol, T., J. R. Rice, J. D. Platt, and J. Suckale (2015), Subglacial hydrology and ice stream
811 margin locations, *Journal of Geophysical Research: Earth Surface*, 120, 1–17, doi:
812 10.1002/2015JF003542.Received.
- 813 Platt, J. D., J. Suckale, T. Perol, and J. R. Rice (2016), Stressing , Hydraulic and Locking
814 Processes at Ice Stream Margins, *Journal of Geophysical Research: Earth Surface, sub-
815 mitted*, 1–23.
- 816 Rathbun, A. P., C. Marone, R. B. Alley, and S. Anandakrishnan (2008), Laboratory study of
817 the frictional rheology of sheared till, *Journal of Geophysical Research*, 113(F02020).
- 818 Raymond, C. (1996), Shear margins in glaciers and ice sheets, *Journal of Glaciology*,
819 42(140), 90–102, doi:10.3198/1996JoG42-140-90-102.
- 820 Raymond, C. (2000), Energy balance of ice streams, *Journal of Glaciology*, 46(155), 665–
821 674.
- 822 Rignot, E., J. Mouginot, and B. Scheuchl (2011), Ice Flow of the Antarctic Ice Sheet, *Sci-
823 ence*, 333, 1427–1431.
- 824 Rignot, E., J. Mouginot, M. Morlighem, H. Seroussi, and B. Scheuchl (2014), Widespread,
825 rapid grounding line retreat of Pine Island, Thwaites, Smith, and Kohler glaciers, West
826 Antarctica, from 1992 to 2011, *Geophysical Research Letters*, 41(10), 3502–3509.
- 827 Ross, N., M. J. Siegert, J. Woodward, A. M. Smith, H. F. Corr, M. J. Bentley, R. C. Hind-
828 marsh, E. C. King, and A. Rivera (2011), Holocene stability of the Amundsen-Weddell ice

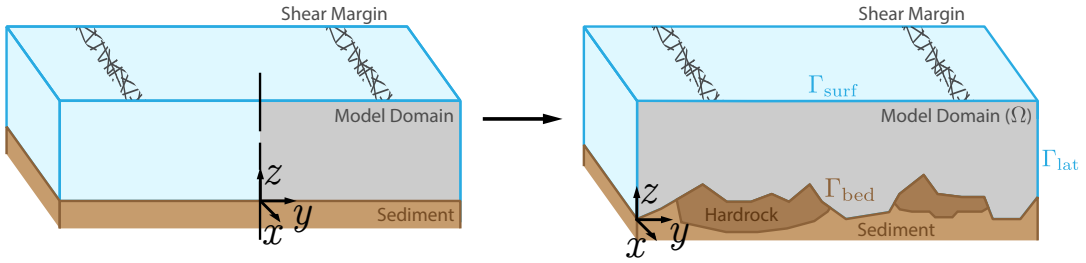
- divide, West Antarctica, *Geology*, 39(10), 935–938, doi:10.1130/G31920.1.
- Ross, N., R. Bingham, H. F. J. Corr, F. Ferraccioli, T. Jordan, A. Le Brocq, D. Rippin, D. Young, D. Blankenship, and M. J. Siegert (2012), Steep reverse bed slope at the grounding line of the Weddell Sea sector in West Antarctica, *Nature Geoscience*, 5(6), 393–396, doi:10.1038/ngeo1468.
- Ross, N., T. A. Jordan, R. G. Bingham, H. F. J. Corr, F. Ferraccioli, A. L. Brocq, D. M. Rippin, A. P. Wright, and M. J. Siegert (2014), The ellsworth subglacial highlands: Inception and retreat of the west Antarctic ice sheet, *Bulletin of the Geological Society of America*, 126(1-2), 3–15, doi:10.1130/B30794.1.
- Rothlisberger, H. (1972), Water Pressure in Intra- and Subglacial Channels, *Journal of Glaciology*, 11(62), 177–203.
- Scambos, T., J. Bohlander, B. Raup, and T. Haran (2004), Glaciological characteristics of Institute Ice Stream using remote sensing, *Antarctic Science*, 16(2), 205–213, doi: 10.1017/S0954102004001919.
- Schoof, C. (2004), On the mechanics of ice-stream shear margins, *Journal of Glaciology*, 50(169), 208–218.
- Schoof, C. (2005), The effect of cavitation on glacier sliding, *Proceedings of the Royal Society A: Mathematical, Physical and Engineering Sciences*, 461(2055), 609–627.
- Schoof, C. (2006a), Variational methods for glacier flow over plastic till, *Journal of Fluid Mechanics*, 555, 299, doi:10.1017/S0022112006009104.
- Schoof, C. (2006b), A variational approach to ice stream flow, *Journal of Fluid Mechanics*, 556, 227, doi:10.1017/S0022112006009591.
- Schoof, C. (2007), Ice sheet grounding line dynamics: Steady states, stability, and hysteresis, *Journal of Geophysical Research*, 112(F3), F03S28, doi:10.1029/2006JF000664.
- Schoof, C. (2012), Thermally driven migration of ice-stream shear margins, *Journal of Fluid Mechanics*, 712(October), 552–578, doi:10.1017/jfm.2012.438.
- Schroeder, D. M., D. D. Blankenship, and D. a. Young (2013), Evidence for a water system transition beneath Thwaites Glacier, West Antarctica., *Proceedings of the National Academy of Sciences of the United States of America*, 110(30), 12,225–8, doi: 10.1073/pnas.1302828110.
- Schroeder, D. M., D. D. Blankenship, D. a. Young, and E. Quartini (2014), Evidence for elevated and spatially variable geothermal flux beneath the West Antarctic Ice Sheet, *Proceedings of the National Academy of Sciences*, 2014, 3–5, doi:10.1073/pnas.1405184111.

- 862 Siegert, M., N. Ross, H. Corr, J. Kingslake, and R. Hindmarsh (2013), Late Holocene ice-
863 flow reconfiguration in the Weddell Sea sector of West Antarctica, *Quaternary Science*
864 *Reviews*, 78, 98–107, doi:10.1016/j.quascirev.2013.08.003.
- 865 Siegert, M. J., N. Ross, J. Li, D. M. Schroeder, D. Rippin, D. Ashmore, R. Bingham, and
866 P. Gogineni (2016), Subglacial controls on the flow of Institute Ice Stream, West Antarc-
867 tica, *Annals of Glaciology*, 57(73), 19–24, doi:10.1017/aog.2016.17.
- 868 Siegfried, M. R., H. A. Fricker, S. P. Carter, and S. Tulaczyk (2016), Episodic ice velocity
869 fluctuations triggered by a subglacial flood in West Antarctica, *Geophysical Research Let-
870 ters*, pp. n/a–n/a, doi:10.1002/2016GL067758.
- 871 Smith, B. E., H. A. Fricker, I. R. Joughin, and T. Slawek (2009), An inventory of active
872 subglacial lakes in Antarctica detected by ICESat (2003–2008, *Journal of Glaciology*,
873 55(192), 573–595, doi:10.3189/002214309789470879.
- 874 Stearns, L. a., B. E. Smith, and G. S. Hamilton (2008), Increased flow speed on a large East
875 Antarctic outlet glacier caused by subglacial floods, *Nature Geoscience*, 1(12), 827–831,
876 doi:10.1038/ngeo356.
- 877 Suckale, J., J. D. Platt, T. Perol, and J. R. Rice (2014), Deformation-induced melting in the
878 margins of the West Antarctic ice streams, *Journal of Geophysical Research: Earth Sur-
879 face*, 119(5), 1004–1025, doi:10.1002/2013JF003008.Flow.
- 880 Thomas, R. (1979), The dynamics of marine ice sheets, *Journal of Glaciology*, 24(90).
- 881 Truffer, M., and K. A. Echelmeyer (2003), Of isbræ and ice streams, *Annals of Glaciology*,
882 36(1996), 66–72.
- 883 Tulaczyk, S., W. B. Kamb, and H. F. Engelhardt (2000), Basal mechanics of Ice Stream B,
884 west Antarctica: 1. Till mechanics, *Journal of Geophysical Research*, 105(1999), 463, doi:
885 10.1029/1999JB900329.
- 886 Weertman, J. (1957), On the sliding of glaciers, *Journal of Glaciology*, doi:10.1007/978-94-
887 015-8705-119.
- 888 Weertman, J. (1974), Stability of the junction of an ice sheet and an ice shelf, *Journal of*
889 *Glaciology*, 13(67), 3–11.
- 890 Winsborrow, M. C. M., C. D. Clark, and C. R. Stokes (2010), What controls
891 the location of ice streams?, *Earth-Science Reviews*, 103(1-2), 45–59, doi:
892 10.1016/j.earscirev.2010.07.003.
- 893 Winter, K., J. Woodward, N. Ross, S. A. Dunning, R. G. Bingham, H. F. J. Corr, and
894 M. J. Siegert (2015), Airborne radar evidence for tributary flow switching in Insti-

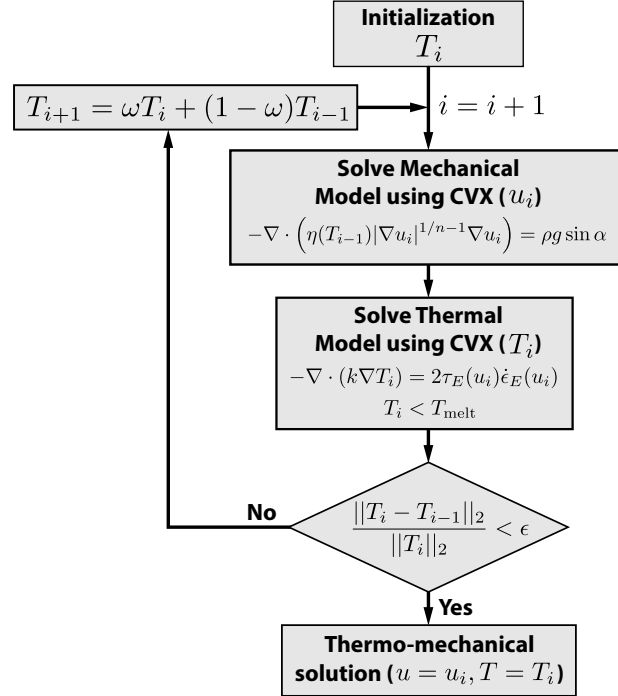
- 895 tute Ice Stream, West Antarctica: Implications for ice sheet configuration and dy-
896 namics, *Journal of Geophysical Research: Earth Surface*, 120, 1611–1625, doi:
897 10.1002/2014JF003432.Received.
- 898 Wright, A., A. Le Brocq, S. Cornford, R. Bingham, H. Corr, F. Ferraccioli, T. Jordan,
899 A. Payne, D. Rippin, N. Ross, et al. (2014), Sensitivity of the weddell sea sector ice
900 streams to sub-shelf melting and surface accumulation, *The Cryosphere*, 8, 2119–2134.
- 901 Zoet, L. K., and N. R. Iverson (2016), Rate-weakening drag during glacier slid-
902 ing *Journal of Geophysical Research : Earth Surface*, pp. 1206–1217, doi:
903 10.1002/2016JF003909.Received.



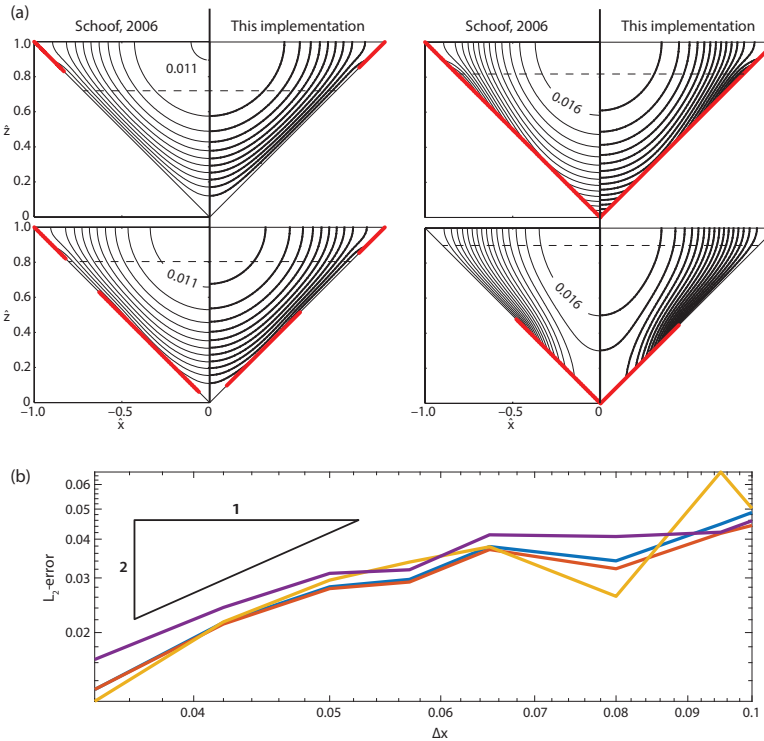
104 **Figure 1.** (a) Map of the study area of Institute Ice Stream, West Antarctica colored by ice speed derived
 105 from satellite radar data from Rignot et al. [2011]. The shear margins are the distinct lateral transitions from
 106 fast to slow flow. The inferred rock-sediment transition from Siegert et al. [2016] is indicated (white line).
 107 Relevant subglacial hydrology is shown in blue, including active subglacial lake [Smith et al., 2009], E1,
 108 hydropotential flow paths [Siegert et al., 2016], and a meltwater channel carved into the ice shelf [LeBrocq
 109 et al., 2013]. Generated with Antarctic Mapping Toolbox [Greene et al., 2017]. (b) Radar cross-section along
 110 C-C' from Siegert et al. [2016], showing basal topography and inferred subglacial conditions. The down-
 111 stream speed (orange line) exhibits distinct differences in the morphology of the two shear margins. Inferred
 112 hydropotential gradients suggest that water flow propagates from the sediment-controlled shear margin to the
 113 hardrock-controlled shear margin.



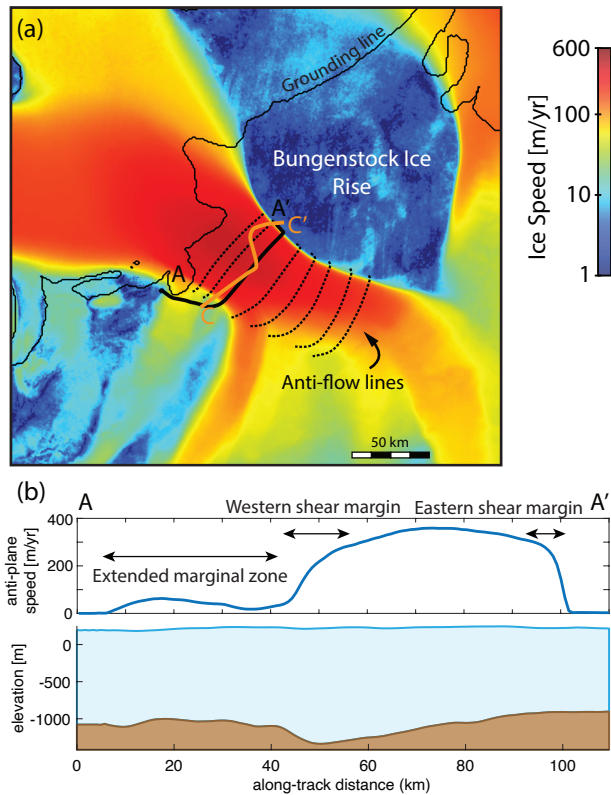
171 **Figure 2.** Schematics of (a) previous, and (b) current model domains. The domain is simplified in previous
 172 models, which focus on the effects of temperature and hydrology. They neglect variations of lithology and
 173 topography at the bed, and considers half of an idealized, symmetric ice stream. The current model focuses
 174 on the effect lithology and topography, and therefore includes the entire ice stream cross-section, variable
 175 lithology, and arbitrary basal topography. Both models neglect variability in along-flow direction, x .



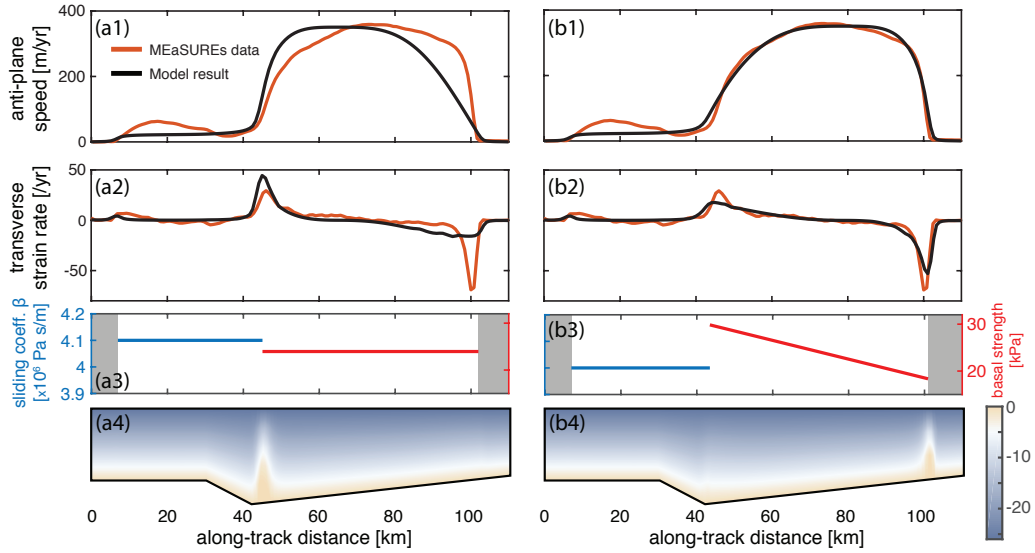
248 **Figure 3.** Flowchart of thermo-mechanical coupling scheme. The mechanical and thermal free-boundary
 249 problems are solved separately using CVX. The coupling is performed with under-relaxation of the tem-
 250 perature field in a Newton-Raphson iteration with the mechanical model. Iterations are performed until the
 251 iteration residual falls below a prescribed value, ϵ .



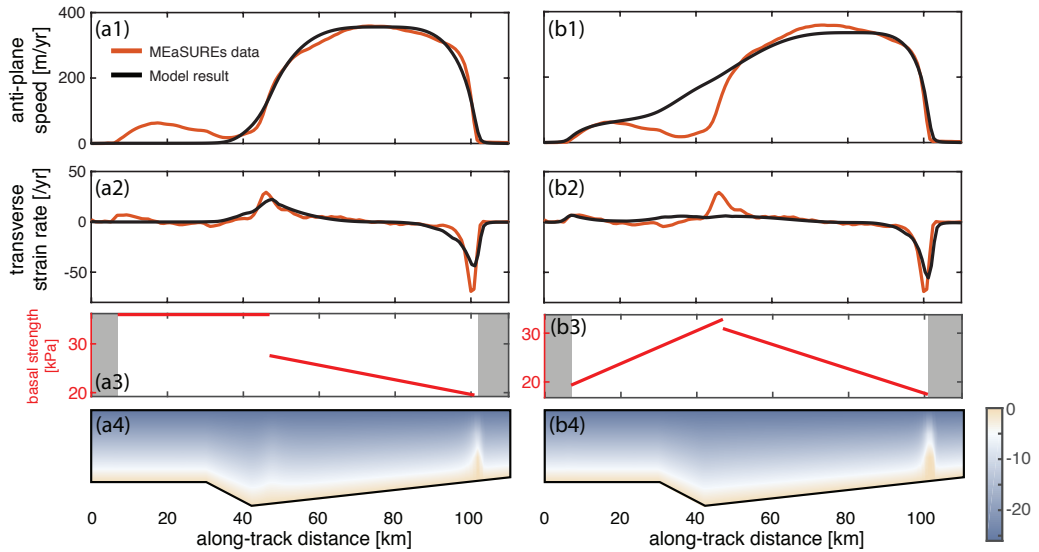
273 **Figure 4.** (a) Benchmarking of the developed method against the implementation by *Schoof* [2006a] for
 274 an idealized valley glacier, reproducing Figure 5 in *Schoof* [2006a]. The dashed line signifies the water table,
 275 with each flow regime chosen to exhibit markedly different regions of till failure (red lines). (b) Convergence
 276 plots of the normalized L_2 -error on surface velocities, computed against most refined solution for each of the
 277 benchmark examples. We observe the expected second-order convergence of linear finite elements, verifying
 278 proper implementation of the model.



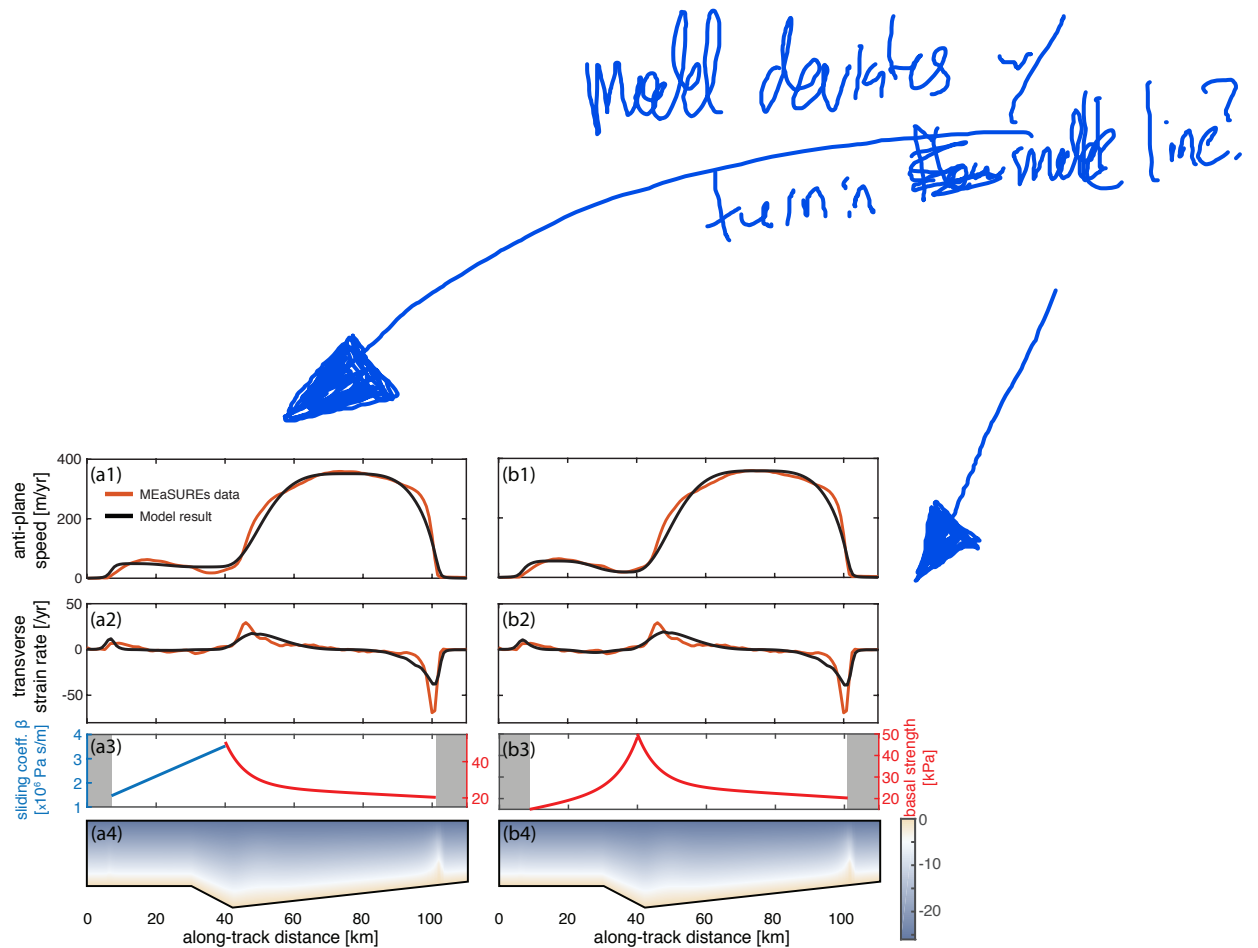
330 **Figure 5.** Map of the study area of Institute Ice Stream, West Antarctica colored by ice speed derived from
 331 satellite radar data from *Rignot et al.* [2011]. The shear margins are the distinct lateral transitions from fast
 332 to slow flow. Generated cross-flowlines are shown as black dashed lines, and cross-flowline A-A' is chosen to
 333 be closest to the radar cross-section along C-C' from *Siegert et al.* [2016]. Generated with Antarctic Mapping
 334 Toolbox [*Greene et al.*, 2017].



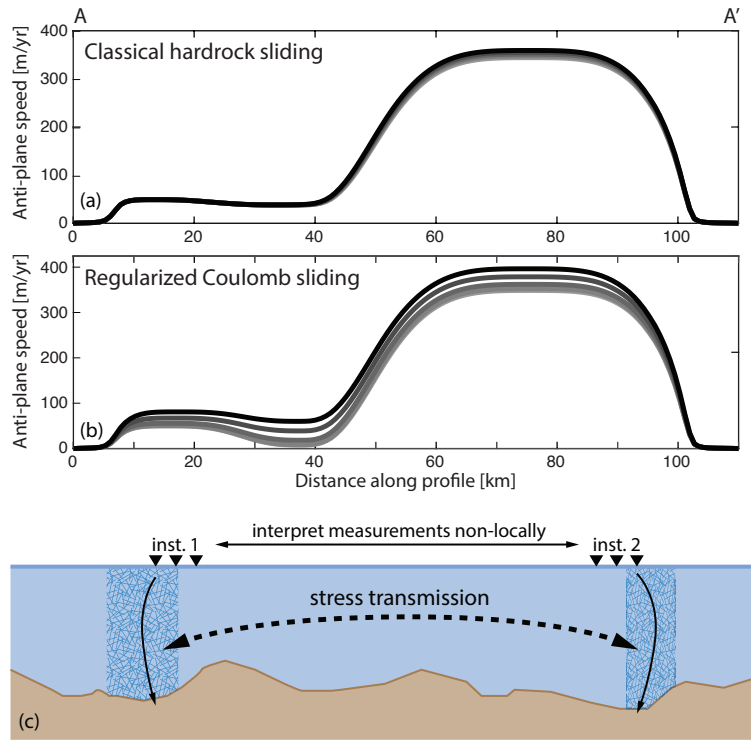
537 **Figure 6.** Numerical experiment investigating spatial variability in sediment strength. (a) Uniform basal
 538 strength in the sediment. (b) Variable basal strength in the sediment as a function of overburden pressure.
 539 Rows illustrate: (1) Comparison of modeled velocities to observed MEaSUREs surface velocities across
 540 profile A-A'. (2) The modeled and observed strain rates across A-A'. (3) Tuned basal conditions, with locations
 541 specified from observations. Hardrock sliding parameter (blue), saturated sediment strength (red), and locked
 542 sediments (gray). (4) Temperature field in the ice column.



543 **Figure 7.** Numerical experiments assuming regularized Coulomb sliding over hard rock and hence a plastic
 544 bed throughout the domain. Simulation (a) assumes a uniform basal strength and (b) a linearly increasing
 545 basal strength in the extended marginal zone. Rows illustrate: (1) Comparison of modeled velocities to ob-
 546 served MEaSUREs surface velocities across profile A-A'. (2) The modeled and observed strain rates across
 547 A-A'. (3) Basal strength of the plastically behaving bed. (4) Temperature field in the ice column.



548 **Figure 8.** Assuming a channel a the hydropotential low with (a) a hardrock ridge and (b) a plastic
 549 ridge. Numerical experiments assuming a meltwater channel in the hydropotential low in the vicinity of
 550 the shear margin with (a) velocity-strengthening sliding over hard rock and (b) regularized Coulomb sliding
 551 implying a plastic bed throughout the domain. Simulation (a) assumes a uniform basal strength and (b) a
 552 linearly increasing basal strength in the extended marginal zone. Rows illustrate: (1) Comparison of modeled
 553 velocities to observed MEaSUREs surface velocities across profile A-A'. (2) The modeled and observed strain
 554 rates across A-A'. (3) Basal strength at the bed with hard rock sliding in blue and the basal strength of a plastic
 555 bed in red. (4) Temperature field in the ice column.



556 **Figure 9.** Modeled velocities across Profile A-A' with a perturbation to channel width for the (a) hardrock
 557 and (b) sediment ridges. We consider a small perturbation of $\Delta\tau_c \approx 1.6$ kPa to the bed strength, which is
 558 commensurate to a few percent of the inferred current-day bed strength τ_c in the immediate vicinity of the
 559 channel. The different lines represent different transient states between the current velocity profile shown in
 560 light grey and the maximum perturbation plotted in black. Panel (c) illustrates the stress transmission occur-
 561 ring in the anti-flow line and highlights that measurements across the entire ice-stream width are necessary to
 562 quantify the shifting force balance.